

A Parallel Adaptive Event Horizon Finder for Numerical Relativity

Andy Bohn^{1,*} and Lawrence E. Kidder, Saul A. Teukolsky¹

¹*Cornell Center for Astrophysics and Planetary Science, Cornell University, Ithaca, New York 14853, USA*

(Dated: October 8, 2018)

With Advanced LIGO detecting the gravitational waves emitted from a pair of merging black holes in late 2015, we have a new perspective into the strong field regime of binary black hole systems. Event horizons are the defining features of such black hole spacetimes. We introduce a new code for locating event horizons in numerical simulations based on a Delaunay triangulation on a topological sphere. The code can automatically refine arbitrary regions of the event horizon surface to find and explore features such as the hole in a toroidal event horizon, as discussed in our companion paper. We also investigate various ways of integrating the geodesic equation and find evolution equations that can be integrated efficiently with high accuracy.

PACS numbers: 04.25.D-, 04.25.dg

I. INTRODUCTION

In late 2015, the Advanced LIGO interferometers detected the gravitational radiation from a pair of merging black holes [1]. This observation gives a unique view into the highly nonlinear regime of compact-object binary mergers, and the observed gravitational waveform is entirely consistent with General Relativity [2]. While numerical relativity simulations help with detecting and analyzing signals that Advanced LIGO receives, they also provide a laboratory for exploring the entire compact object coalescence parameter space, including the 7-dimensional space of binary black hole (BBH) mergers. Algorithmic improvements in addition to increasing computational power over time have led to a large surge in the number of BBH simulations available to the community [3–8].

Among the properties of the spacetime that can be studied using numerical simulations, perhaps the most interesting are those of black hole *event horizons* (EH), the boundaries of the causal past of future null infinity. The EH surface is therefore dependent on the entire future of the spacetime, making it impossible to locate during BBH simulations that progress forwards in time. A similar surface, called the *apparent horizon* (AH), is the boundary between outward directed light rays moving away from or toward the center of the black hole. In particular, the EH always contains the AH if it exists, and the surfaces are equal if the black hole has settled down to equilibrium. Locating an AH at a certain time requires only information at that time, so AHs are commonly located during BBH simulations as an EH substitute. Even though EHs are more difficult to locate, we are interested in how to find them because they define the surface of black holes, and physical properties such as the mass and angular momentum of black holes are determined by integrations over the event horizon surface [9].

We locate event horizons in BBH mergers by utilizing

a theorem that the event horizon is generated by null geodesics having no future end point [10–12]. Long after the black holes have merged, the spacetime settles down to Kerr, where the EH is identical to the AH. So we can select a set of outgoing null geodesics that lie on the apparent horizon of the remnant black hole near the end of the BBH simulation [13] and integrate the geodesics backwards through time [13–19]. The convention that we will follow in this paper is to call these geodesics event horizon generators, though they are only very good approximations to the true generators [19]. Although generators of the horizon have no future endpoint, while tracing the generators backwards in time, some may “leave” the event horizon surface where they meet other generators of the horizon. These points are called *caustics* when infinitesimally neighboring generators join together, and *crossover points* when non-neighboring generators cross paths [16, 19–22]. After they leave the event horizon surface backwards in time, generators are known as *future generators* of the horizon. When viewing the event horizon forwards in time, future generators become generators of the event horizon after they join through either caustics or crossover points.

The previous generation of event horizon finding code in SPEC [18, 19] was sufficient to locate event horizons reasonably accurately, but lacked the ability to adaptively refine itself to study small scale features of the EH surface. An example of a small scale feature we are interested in exploring is a topological hole through the event horizon surface, causing the EH topology to be toroidal. The companion to this paper [23] focuses on locating such short-lived toroidal event horizons. This paper outlines the details behind our new event horizon finder, and the adaptive refinement tools that are essential to resolve a toroidal event horizon.

The organization of this paper is as follows: In Section II we give an overview of the backwards geodesic method for locating event horizons. In Section III we present the Delaunay triangulation [24, 25] on a spherical topology that we use to represent the event horizon surface, allowing for adaptive refinement. In Section IV and Section V, we show efficient null geodesic evolution

* Contact email: adb228@cornell.edu

equations and outline how we handle metric data during generator evolution. In Section VI, we describe the initial data calculation for event horizon generators, and in Section VII we describe how we identify future generators during the backwards in time evolution.

II. BACKWARDS GEODESIC METHOD OVERVIEW

Cohen *et al.* [18] compared three methods for locating event horizons and found the most robust method to be the backwards geodesic method. We follow this approach, where we evolve a set of event horizon generators backwards in time to trace out the EH surface. The generators are outward null geodesics that exponentially converge to the true EH surface when traced backwards through time. As we will discuss in Section III, we connect the generators together to form a polygon approximating a smooth surface with the topology of a sphere that may be self-intersecting. This surface does not approximate the event horizon only, but represents the union of the true event horizon and the locus of future generators [26].

To make the discussion concrete, consider a head-on equal mass binary black hole merger, shown in Fig. 1. We see spatial cross-sections of apparent horizon surfaces shown blue or green, event horizon surfaces shown in orange, and the future generator surface shown in translucent purple. In panel (a), sufficiently long before the merger, the event horizon surfaces are almost identical to the blue apparent horizon surfaces, which are hardly visible at this time. The future generator surface consists of future generators that will join onto the event horizon surface in the future. When rotating this panel about the rotational axis of symmetry, the union of the event horizon surfaces and future generator surface forms a smooth topological sphere. In panel (b), shortly before the merger, the future generator surface is smaller because some of the future generators joined the event horizon between this panel and the previous panel. We can see the difference between the AH and EH surfaces increases as we get closer to the merger. There are no more future generators in panel (c) since they have all joined the event horizon surface.

In panel (d), a common apparent horizon shown in green has formed around the two interior apparent horizons, and all three apparent horizons lie entirely on or within the event horizon, as they should. As time progresses to panels (e) and (f), we stop tracking the blue inner apparent horizons, the EH settles to a stationary state, and the common AH approaches the event horizon until the two surfaces eventually coincide. With this picture in mind, the method used to locate the EH is to evolve generators backwards in time from panel (f) toward panel (a), which traces out the union of the event horizon surface with the future generator surface. Backwards in time, some generators “leave” the event horizon surface as seen in panels (b) and (a), so we must be able to identify

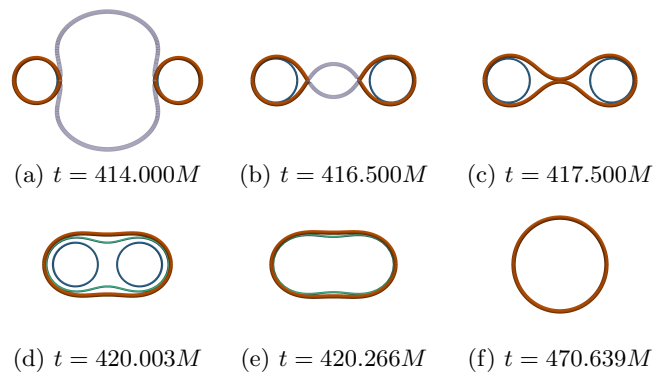


FIG. 1. Cross-sections through apparent horizons and the locus of event horizon generators for a head-on BBH merger, similar to Fig. 1 of [18]. Shown in translucent purple are future generators of the horizon that continuously merge onto the event horizon, shown in orange, until the merger in panel (c). Shown as blue curves in panels (a-d) are apparent horizons associated with the two individual black holes, and shown as a green curve in panels (d-f) is a common apparent horizon.

which generators leave the surface and when they leave.

III. EVENT HORIZON REPRESENTATION

One of the shortcomings of our previous event horizon finder was the lack of flexibility in refining the distribution of event horizon generators in certain regions of interest. The method of distributing event horizon generators in Cohen *et al.* [18] used collocation points in a spherical harmonic ($Y_{lm}(u, v)$) expansion, with u values chosen so that $\cos u$ were the roots of the Legendre polynomial of order $L + 1$, and v values uniformly distributed in $[0, 2\pi)$, yielding $2(L + 1)^2$ generators. This results in the generators not being distributed evenly over the event horizon surface, and does not allow one to increase the resolution of a small patch of the surface.

We want to be able to evenly distribute event horizon generators over the event horizon as well as to be able to adaptively refine regions of the surface to sufficiently resolve the small scale features of the merger. Compared to other methods of locating event horizons [18], the backwards geodesic method allows simple adaptive refinement, in that we only need to add more generators wherever we want to refine. In addition to being able to place generators where desired, we require of our EH representation the ability to connect the generators to approximate a smooth surface.

To establish an initially evenly distributed set of generators, we begin with a regular icosahedron inscribing a unit sphere as seen in the first panel of Fig. 2. This corresponds to our base resolution with 12 vertices and 20 triangles. The triangular faces of the icosahedron form a triangulation over the sphere, where each vertex corresponds to one generator of the event horizon. We will see later in Section VI exactly how we map from this sphere

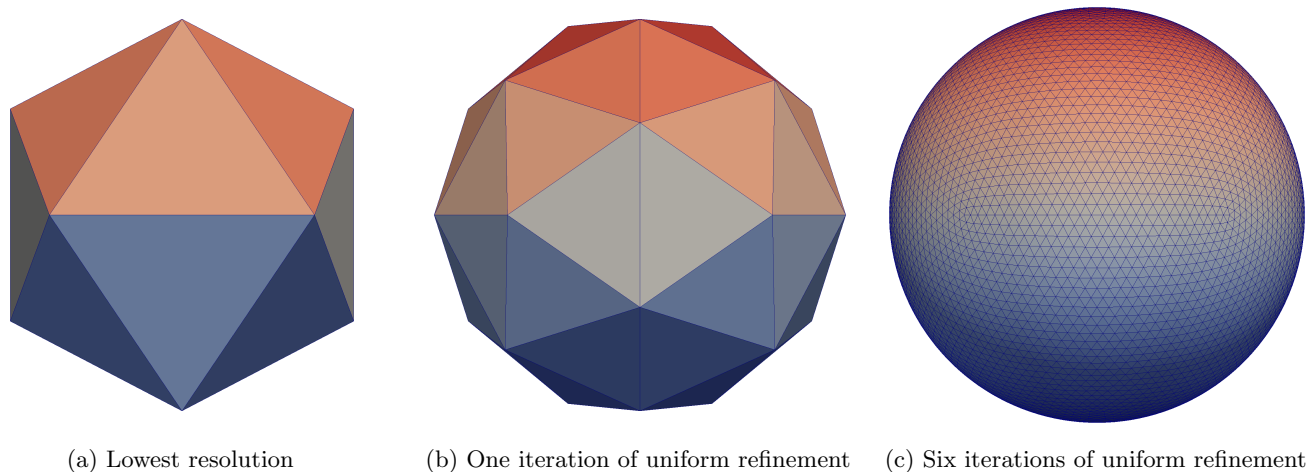


FIG. 2. Varying resolutions of a triangulation over the unit sphere used during initial data generation. The lowest resolution has 12 vertices and 20 triangles evenly distributed over the sphere. One iteration of uniform refinement leads to a triangulation with 32 vertices and 60 triangles. Six iterations results in 7,292 vertices.

to event horizon generators, but for now consider this to closely represent the distribution of generators over an event horizon.

We can reach arbitrarily high resolutions by applying the following triangle refinement procedure to each of the 20 triangles on the surface:

1. Choose a point at the median of the vertices of the triangle to be refined.
2. Move the point radially outward to the surface of the unit sphere.
3. Convert the original triangle to three smaller triangles by connecting the new point with the vertices of the original triangle.
4. Check the Delaunay condition, described below, along all exterior edges of the new triangles and perform an edge flip if necessary.

When we apply this procedure to all the triangles, we call it *uniform refinement*.

To understand the Delaunay condition and edge flips, consider four points connected to form the quadrilateral $\square ABCD$. There are two ways to form a set of two triangles from this quadrilateral, either by connecting \overline{AC} to form $\triangle ABC$ and $\triangle ACD$, or connecting \overline{BD} to form $\triangle ABD$ and $\triangle BCD$. The pair of triangles with the largest minimum angle among the six interior angles satisfies the Delaunay condition. An edge flip is the name for the process of converting a pair of triangles with a shared edge that fails the Delaunay condition into one that satisfies the condition. For example, we could “flip the edge” \overline{AC} by removing \overline{AC} and replacing it with \overline{BD} .

There are two choices for how to calculate the interior angles of these triangles, since the triangle vertices live on a sphere. The code can handle treating the triangles as either flat or curved along the surface of the sphere. We

default to treating the triangles as curved when calculating angles, but this difference becomes less important as the triangles get sufficiently small.

One round of uniform refinement adds a vertex to each triangle, going from an icosahedron with 12 vertices to a Pentakis dodecahedron with 32 vertices shown in panel (b) of Fig. 2. This procedure can be repeated indefinitely, but we typically uniformly refine the full triangulation six times, resulting in 7,292 vertices evenly distributed over the surface as shown in panel (c) of Fig. 2. In general, the n^{th} iteration of uniform refinement has 20×3^n triangles and $2 + 10 \times 3^n$ vertices¹.

While there are faster ways to generate uniform distributions of vertices over the sphere, the refinement method we use is general and can be used to adaptively refine arbitrary regions of the sphere by only refining a subset of the triangles, a procedure we call *selective refinement*. In practice, we typically do a pilot event horizon run using a uniform distribution of 7,292 generators to determine the set of triangles we are interested in refining. Then we add generators to only those triangles in the region of interest and perform a second event horizon run. Selective refinement is crucial for studying small-scale features of the event horizon, such as the short-lived hole in a toroidal EH surface as discussed in the companion paper [23].

We have control over multiple parameters to tune the selective refinement:

- The *refinement depth* parameter roughly controls how many points are added to the selected triangles.
- The *refinement width* parameter controls how wide a region we are refining.

¹ Every iteration of uniform refinement adds one vertex per triangle in the triangulation, so we have $12 + 20 \sum_{i=1}^n 3^{i-1}$ vertices at the n^{th} level of refinement.

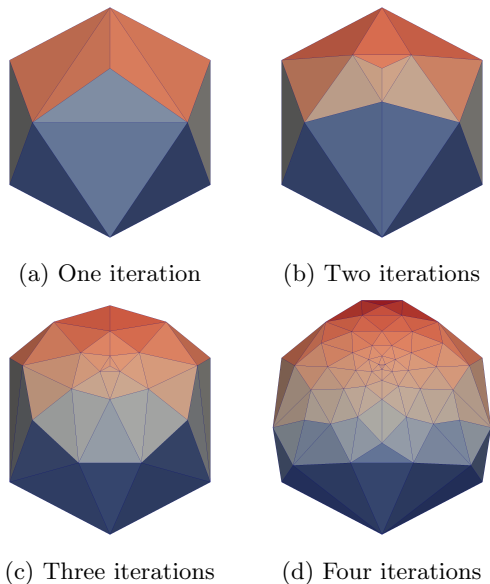


FIG. 3. Selective refinement of one triangle in the original 12 vertex triangulation shown in Fig. 2. Panels (a)-(d) show one to four iterations of our refinement procedure applied to one triangle.

- We can control how many event horizon iterations we perform.

The refinement depth and width provide complete control over the refinement for the problems we are interested in, so we usually set the number of EH runs to two, corresponding to one round of refinement.

Before seeing examples of localized refinement, we must introduce the concept of a triangle *descendant*. When refining one triangle, we add a vertex and convert the triangle to three new triangles that are all labeled descendants of the original triangle. In addition, if we have to perform any edge flips, we convert two triangles into two new triangles that are both labeled descendants of the two previous triangles. We maintain a full tree-like structure of triangles that is useful for quickly locating triangles given a location on the sphere, but more importantly the tree is useful when adding more than one point to a triangle.

An example of selective refinement is shown in Fig. 3, where we explore aggressive refinement of one triangle. Panel (a) shows one refinement iteration applied to one triangle, where a point is added and connected to the vertices of the triangle. The Delaunay condition is checked on all 3 edges opposite the new vertex, but in this instance, no edges needed to be flipped. In panel (b), to reach a second refinement iteration we add a point to each of the three previously created triangles, resulting in a total of 4 new points. In other words, we add a vertex to each descendant of the original triangle. Again the Delaunay condition is checked on the edges opposing any of the new vertices, which is 6 edges in this case. We can see that all 6 edges are flipped here, giving an

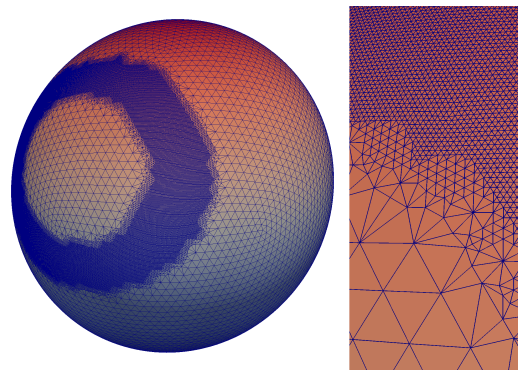


FIG. 4. Selective refinement of event horizon generators for a BBH with mass ratio 6, refining from 7,292 generators to 49,350 generators. The right section of the figure shows a zoomed-in region of the left section, highlighting the smooth transition of generator density over the initial data surface. The regions where refinement occurs are chosen to be around the generators associated with the neck of the event horizon during the BBH merger, as seen in Fig. 5.

improved set of triangles. To perform a third refinement iteration, we must again add one vertex to each of the 12 descendant triangles of the original triangle and check for edge flips. The refinement depth is closely related to the number of refinement iterations. Our highest resolution event horizon run to date refined from 7,292 to 246,687 generators with this procedure, and the algorithm handles this with no problems.

Performing edge flips continually as we refine is important because we add points to the median of each triangle. If we want an even distribution of vertices, then we want each triangle to be as close to equilateral as possible, which amounts to maintaining a Delaunay condition on the sphere. These edge flips allow the density of vertices to change smoothly even though there is a large range of vertex densities over the sphere, as seen by comparing the density of vertices in panel (d) of Fig. 3 to the original vertices in Fig. 2. In practice, the refinement does not stray far beyond the region where we are interested in refining.

Figure 4 shows an example of selective refinement of an event horizon surface for a binary. The surface is the initial data surface for an event horizon simulation of a 6 to 1 mass ratio binary, with dimensionless spin $\chi \approx 0.9$ on the large BH and $\chi \approx 0.3$ on the small BH in arbitrary directions ([4] ID SXS:BBH:0165). To study the small scale features that arise where the event horizons first touch, we need to add generators to that portion of the surface. The right side of this figure shows a zoomed-in region of the event horizon surface to illustrate the transition between the low resolution and high resolution regions. Figure 5 shows the same simulation during the merger, where we can see the high density of event horizon generators located in the neck of the event horizon where the black holes met slightly earlier.

The density of generators is smooth and continuous

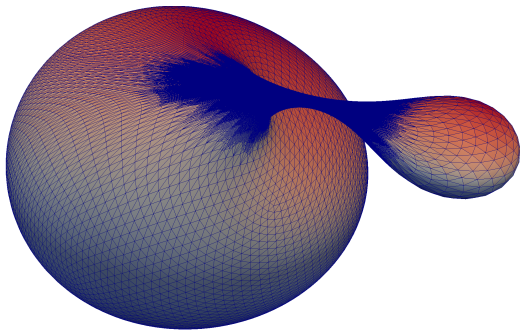


FIG. 5. Generator locations during the merger of a 6 to 1 mass ratio binary, for which initial data is shown in Fig. 4. Refinement occurs in the neck of the event horizon, where future generators joined the event horizon surface earlier in the merger.

between the low density and high density regions of generators. This good behavior arises partially from continually checking the Delaunay condition, as seen in Fig. 3. In addition, the code sets the number of refinement iterations to smoothly transition between the low and high density regions automatically. While our selective refinement algorithm refines triangles, we determine which triangles to refine based on whether the generators at the vertices of the triangle were future generators in the past. If only one vertex of a triangle satisfies this property, then we set the number of refinement iterations to the specified refinement depth. For each additional vertex of that triangle associated with the neck region, we increment the number of refinement iterations by one. For example, if the refinement depth parameter is set to 3, as in Fig. 4 and Fig. 5, then we refine triangles along the border of the refinement region 3 or 4 iterations, and triangles in the interior 5 iterations.

The other tunable parameter is the refinement width, which controls how wide our refinement region is. Using Fig. 1 as a reference, if we refined triangles associated with the future generators in panel (b) we would obtain a fairly thin refinement region, but if we refine based on the future generators in panel (a) we would widen the refinement region. Therefore we control the refinement width by choosing how long before the merger we identify triangles associated with future generators.

The parameters discussed so far refine the neck of the event horizon satisfactorily, but refine nowhere else. For high mass ratio binaries, such as the one shown in Fig. 5, it may be worthwhile to consider refining the surface based on the curvature as well. In this case, the smaller black hole would have a large curvature compared to the number of generators in the region, and thus would have more generators added to that region. One way to accomplish this refinement is to look at the angle between the normal of a triangle and the normal of all its neighboring triangles, and add generators if the angle is too large. This type of refinement is not currently implemented since we are only interested in the neck region for this paper.

After assembling a useful distribution of generators on the EH, how do we calculate quantities over the surface? Derivatives of scalars are calculated using first-order finite differencing, following [27] adapted to a curved surface. For some scalar f defined at the vertices of the triangulation, we can approximate the derivatives of the scalar inside the triangle using the function values at the vertices

$$\partial_\theta f \approx [(\phi_2 - \phi_3)f_1 + (\phi_3 - \phi_1)f_2 + (\phi_1 - \phi_2)f_3] / \Delta \quad (1a)$$

$$\partial_\phi f \approx -[(\theta_2 - \theta_3)f_1 + (\theta_3 - \theta_1)f_2 + (\theta_1 - \theta_2)f_3] / \Delta \quad (1b)$$

$$\Delta = (\phi_2 - \phi_3)\theta_1 + (\phi_3 - \phi_1)\theta_2 + (\phi_1 - \phi_2)\theta_3, \quad (1c)$$

as in equation (1) of [27], where f_i is the scalar value at the vertex with coordinates (θ_i, ϕ_i) , $\partial_u f$ is the partial derivative of f with respect to u , and Δ is twice the coordinate area of the triangle. To evaluate the derivative at a vertex, we perform a weighted average of Eq. (1a) over each triangle the vertex belongs to. The derivative of the scalar at a vertex can thus be approximated as

$$\partial_\theta f \approx \sum_{i=1}^N (\phi_{i+1} - \phi_{i-1})f_i / \Delta \quad (2a)$$

$$\partial_\phi f \approx \frac{1}{\sin \theta} \sum_{i=1}^N (\theta_{i+1} - \theta_{i-1})f_i / \Delta \quad (2b)$$

$$\Delta = \sum_{i=1}^N (\phi_{i+1} - \phi_{i-1})\theta_i. \quad (2c)$$

The derivatives in Eq. (2a) are well-behaved far from the poles of the (θ, ϕ) coordinate system, but would require care when crossing the poles. Since our choice of vertices is evenly spread over the sphere, the vertices do not avoid the coordinate singularity at these poles. To obtain well-behaved derivatives everywhere, we set up three (θ, ϕ) coordinate systems on the sphere with the poles on the x , y , or z axis, using a cyclic permutation of the usual Cartesian to spherical coordinate transformation. The derivative at some vertex uses all neighboring vertices, so the lowest resolution triangulation our code supports must be oriented such that each vertex and its neighbors live entirely in one of the three coordinate systems without crossing the poles. This corresponds to vertices at all cyclic permutations of $(\pm\phi, \pm 1, 0) / (\sqrt{1 + \phi^2})$, where ϕ is the golden ratio, and we have normalized to 1. When computing quantities that do not depend explicitly on the choice of coordinate system on the sphere, we simply choose the coordinate system farthest from the poles, i.e. θ closest to $\pi/2$.

IV. GENERATOR EVOLUTION

Our code can trace event horizon generators independently through either numerical or analytic metric data,

which is useful for performing code tests. It is common for numerical simulations to use the 3+1 decomposition [28], so we express the metric in the form

$$ds^2 = -\alpha^2 dt^2 + \gamma_{ij}(dx^i + \beta^i dt)(dx^j + \beta^j dt), \quad (3)$$

where α is the lapse function, β^i is the shift vector, and γ_{ij} is the spatial metric.² We obtain numerical data from simulations performed using the Spectral Einstein Code (SPEC) [4, 29–31]. The generators are traced by evolving a solution to the geodesic equation

$$\frac{d^2 x^\tau}{d\lambda^2} + \Gamma^\tau_{\mu\nu} \frac{dx^\mu}{d\lambda} \frac{dx^\nu}{d\lambda} = 0, \quad (4)$$

where x^τ is the four-position of the geodesic, λ is an affine parameter, and $\Gamma^\tau_{\mu\nu}$ are the Christoffel symbols describing the effective force caused by spacetime curvature.

To facilitate the numerical geodesic evolution, we split this second-order differential equation into two first-order equations using an intermediate momentum-like variable such as $p^\tau = dx^\tau/d\lambda$. As we have some freedom in the definition of this momentum variable, we look for one that helps to minimize computational time and numerical errors when evolving through spacetimes with black holes.

We initially explored using the variable $p_\tau = dx_\tau/d\lambda$ from Hughes *et al.* [15], along with converting the evolu-

tion equations from affine parameter λ to the coordinate time t of SPEC evolutions through the use of $p^0 = dt/d\lambda$. Although the resulting evolution equations are concise and have no time derivatives of metric variables, the quantities p^0 and p_i grow exponentially near black hole horizons in typical coordinate systems used by SPEC simulations. This forces our time-stepper to take prohibitively small steps in order to achieve the desired accuracy.

We therefore choose a momentum variable slightly different than p_τ to mitigate this time-stepping problem. Null geodesics satisfy $\vec{p} \cdot \vec{p} = 0$, which can be rewritten as $p^0 = \alpha^{-1}(\gamma^{ij}p_i p_j)^{1/2}$ using the metric in Eq. (3). This expression shows that p^0 and p_i scale similarly, so we can eliminate the exponential behavior of these variables by evolving the ratio. Our intermediate variable thus becomes

$$\Pi_i \equiv \frac{p_i}{\alpha p^0} = \frac{p_i}{\sqrt{\gamma^{jk} p_j p_k}}, \quad (5)$$

where we also divide by α to reduce the number of terms in the resulting evolution equations. This choice of intermediate variable is the same one that appears in [32]. Using Π_i and the 3+1 decomposition of Eq. (3), we can express the geodesic equation in Eq. (4) in the form

$$\frac{d\Pi_i}{dt} = -\alpha_{,i} + (\alpha_{,j}\Pi^j - \alpha K_{jk}\Pi^j\Pi^k)\Pi_i + \beta^k_{,i}\Pi_k - \frac{1}{2}\alpha\gamma^{jk}_{,i}\Pi_j\Pi_k \quad (6a)$$

$$\frac{dx^i}{dt} = \alpha\Pi^i - \beta^i, \quad (6b)$$

where K_{jk} is the extrinsic curvature (see, e.g., [28]) and Π^i is defined via the inverse spatial metric as $\Pi^i \equiv \gamma^{ij}\Pi_j$. Note that the geodesic equation consists of four second-order equations, yet we only have three pairs of coupled first-order equations in Eq. (6b). Because we are evolving a normalized momentum, Eq. (5), we have lost information about p^0 during evolution. Compared to the evolution equations in Hughes *et al.* [15], we have introduced a time derivative of the three-metric inside K_{jk} , but we have significantly sped up the evolution near black holes by removing the exponential growth of p^0 and p_i .

The equations in Eq. (6b) are similar to those in (28) of Vincent *et al.* [33]. In fact our intermediate evolution variable Π_i is related to their variable V^i by the three-metric, such that $\Pi^i = V^i$. But our Eq. (6b) has a reduced number of both temporal and spatial derivatives of metric

quantities compared to Vincent's (28). More detailed information about splittings of the geodesic evolution equation can be found in Appendix A.

V. HANDLING METRIC DATA

Because we perform the generator evolution through the SPEC metric data backwards in time, we must complete the binary black hole simulation beforehand while saving sufficient metric data to disk. We need all the metric components specified in Eq. (6b) at any given time and location in the evolution domain, or we need to be able to compute them. While we do not need all of the metric and its derivatives in our evolution equations, it is simpler to save $g_{\mu\nu}$ and all of the derivatives used during the SPEC BBH simulation and deal with slightly more disk space usage.

The metric and derivatives are stored on the BBH evolution grid points at a deterministic set of times such that we can interpolate the metric quantities to any spacetime

² Our convention is that Greek indices, as in x^τ , denote temporal or spatial components, while Latin indices, as in x^i , denote only spatial components.

point in the simulation domain. The metric $g_{\mu\nu}$ has 10 unique components when accounting for symmetry, and the derivatives $\partial_\delta g_{\mu\nu}$ have 40 components leading to a total of $50N_{\text{pts}}N_t$ numbers, where N_{pts} is the average number of grid points and N_t is the number of time slices stored. In addition, some extra information about where the points are located and how they are distributed must also be stored.

For one fully generic BBH evolution of unequal mass black holes with arbitrary spin directions and magnitudes, the metric data can take many terrabytes of disk usage. Since typical clusters have one or two gigabytes of memory per core, we do not have nearly enough memory to read all the metric data at once. To handle this situation, we utilize a shared memory paradigm by using OpenMP. During generator evolution, we read sections of the metric data into memory only as needed and at most once, storing it in a shared thread-safe cache. Other generators then simply access the cache to get the metric data instead of reading it from disk for themselves.

We maintain a priority queue of generators ordered by their current evolution time, such that generators that are farthest behind are given highest priority. After a pool of OpenMP threads is spawned, each thread will grab the next highest priority generator in the queue, evolve for one timestep, then insert the generator back into the priority queue. A potential concern that the CPU cache was not being utilized by taking only one timestep at a time turned out not to be valid. With the priority queue, generators are kept as close in time as possible, so that metric data in the cache is kept for as little time as needed. Since the domain structure in SPEC consists of many subdomains, only the required subdomains are read into memory. Periodically, we use the evolution time of the farthest-behind generator to determine which metric data stored in the cache is safe to be deleted³.

When a generator requests metric data at a particular location and time, we must perform both a spatial and a temporal interpolation in general. Spatial interpolations are performed spectrally, taking advantage of the pseudo-spectral grid used during SPEC simulations. We are left with the innocent looking tasks of temporal interpolation and how to properly combine temporal and spatial interpolations. These tasks turn out to be quite complicated and are described in Appendix B.

VI. INITIAL DATA

We evolve a set of event horizon generators backwards in time to trace the event horizon surface, so we need

to set an initial time, location, and direction for each generator. As hinted at by Fig. 1, the apparent horizon and event horizon surfaces asymptotically approach each other after the merger. If we set the initial time of the backwards evolution to be late enough, the black hole will have settled to a nearly stationary solution and the apparent horizon surface could be used as initial data for the locations of the event horizon generators [13]. In SPEC, the apparent horizon is represented with a spherical harmonic decomposition, so we simply look for a time where the spherical harmonic coefficients are sufficiently stationary to choose an initial time.

Next we need to determine the positions of the generators using the triangulation over the unit sphere described in Section III. We first note that each vertex of the unit sphere triangulation defines a (θ, ϕ) direction. The position of the generator associated with that vertex is then set to the intersection of the AH surface and the ray starting at the center of the AH pointing in the direction defined by the vertex. We use spectral interpolation on the spherical harmonic basis used to represent the AH to find the intersection. Since stationary black hole AHs have a nearly spherical shape when represented in typical coordinate systems used by SPEC, mapping between the reference sphere and the AH surface roughly maintains the carefully constructed distribution of vertices from Section III.

Finally, we need to find the initial direction of each generator, used to calculate our intermediate evolution variable $p_i/(\alpha p^0)$ from Eq. (6b). Following [18], the initial direction of a generator should be the normal to the surface at the location of the generator, where the normal is calculated spectrally on the AH following Baumgarte *et al.* [34]. The normal direction is set to p^i , which is transformed into $p_i/(\alpha p^0)$ using the lapse and p^0 as calculated in Section IV.

It is important to note that refinement of the unit sphere in Section III never destroys vertices, but only destroys (and then creates) triangles. Once we trace an EH generator trajectory, we can store and reuse the trajectory after refinement without retracing the generator. Therefore we only calculate initial data for newly created vertices in the triangulation for which we need to find the trajectory. Unfortunately, while the generator trajectories from the pilot run do not need to be recalculated, determining when generators join the horizon must be recalculated completely since the triangles have changed.

VII. IDENTIFYING FUTURE GENERATORS

Although the event horizon surface is generated by null geodesics that never leave the horizon, event horizon generators readily join onto the horizon during the merger, as can be seen in Fig. 1. In the backwards in time language, generators can leave the horizon where they meet other generators through one of two types of points: caustics, where neighboring generators converge to a point, or

³ Given that the farthest-behind generator is at time t , determining which metric data times are safe to delete is more complicated than just comparing the stored times against t . This is because we need to perform time interpolation, so the interpolation stencil width is also a factor.

crossover points, where non-neighboring generators on the horizon meet. We must therefore identify and distinguish these caustics and crossover points.

When we trace event horizon generators, we record their locations at a predetermined set of times. In order to properly resolve the short-duration features appearing during the merger of the black holes, we need fine time resolution during the merger. However, the process of looking for caustics or crossover points scales linearly

$$\Delta t(t) = \begin{cases} \Delta t_{\text{coarse}} + (\Delta t_{\text{fine}} - \Delta t_{\text{coarse}}) \times \left[0.5 \left(1 + \tanh \left(\frac{\Delta t_{\text{coarse}}}{\Delta t_{\text{fine}}} \left\{ \tan \left(\pi \left(1.5 - \frac{t - t_{\text{begin}}}{t_{\text{fine}} - t_{\text{coarse}}} \right) \right) \right\} \right) \right) \right] & t_{\text{coarse}} \leq t \\ \Delta t_{\text{coarse}} & t_{\text{fine}} \leq t < t_{\text{coarse}} \\ \Delta t_{\text{fine}} & t < t_{\text{fine}} , \end{cases} \quad (7)$$

where Δt_{fine} and Δt_{coarse} specify the fine and coarse spacings, t_{fine} and t_{coarse} specify the boundaries for the fine and coarse spacing regions, and the transition function in square brackets varies between 0 and 1. The time range between t_{fine} and t_{coarse} is used to smoothly transition between the different spacings, and any smooth monotonic transition function would be sufficient.

After performing the tracing, we must determine if and when generators leave the horizon backwards in time using the recorded generator locations. We search for caustics, where neighboring generators meet, by looking for generators with negative expansion parameter, similar to Cohen *et al.* [18]. The expansion of a generator is proportional to the fractional change of the area element around the generator,

$$\theta \propto \frac{1}{\sqrt{h}} \frac{\partial \sqrt{h}}{\partial t}, \quad (8)$$

where h is the determinant of the induced metric on the horizon at the location of the generator. Unlike Cohen *et al.* [18], where the induced metric is found using second-order finite difference stencils, it is not trivial to go beyond first-order finite differencing using our irregularly structured grid. Nevertheless, we see no evidence that the first-order derivatives are not accurate enough, since the adaptive refinement scheme discussed in Section III drastically decreases the distance between generators.

The induced metric on the event horizon is given by

$$h_{ab} = \gamma_{ij} \frac{\partial q^i}{\partial y^a} \frac{\partial q^j}{\partial y^b}, \quad (9)$$

where γ_{ij} is the spatial metric, q^i are the coordinates on the 3-dimensional spacetime slice, and y^a are the (θ, ϕ) coordinates on the horizon surface. The derivatives are calculated using Eq. (2a). Since we are only interested in the fractional change in $\sqrt{\det h_{ab}}$ in Eq. (8), we are free to perform a useful rescaling of the induced metric such

with the number of times where we record generator locations. We do not require such fine time resolution after merger where the event horizon is slowly varying and no more generators are joining, so we smoothly transition the separation between recording times from the fine resolution merger to the coarse resolution ringdown. We use a piecewise function with a hyperbolic tangent transition function to specify the spacing between recording times Δt ,

that

$$\tilde{h} = \det \tilde{h}_{ab} = \frac{1}{\sin^2 \theta} \det h_{ab}. \quad (10)$$

For a spherically symmetric space, \tilde{h} is a constant over the sphere, which provides a useful correctness check and removes the coordinate dependence on θ .

When computing derivatives on the event horizon surface, to avoid coordinate issues around the poles of the coordinate system, we can align the poles with the x , y , or z axes by choosing the corresponding coordinate system defined in Section III. We are free to change coordinate systems when calculating the expansion for different generators since we are not comparing neighboring generators, but only checking the sign of the expansion parameter.

To find the specific time t_{join} that a generator joins on the horizon, we first compute $\sqrt{\tilde{h}}$ for each generator at each stored time. Then we take the partial derivative with respect to time along each generator with a third order Lagrange interpolating polynomial and calculate the fractional change of $\sqrt{\tilde{h}}$ with respect to time, which is proportional to the expansion parameter. If this fractional change with respect to time changes sign between two recording times, we know the join time is between these times. We identify t_{join} by simply linearly interpolating the fractional change between the recording times where it changes sign to find when the expansion parameter passes through zero.

This algorithm to compute the expansion is parallelized using a set of MPI processes and a pool of OpenMP threads on each process. The set of generators on the event horizon surface is distributed evenly across the OpenMP threads and MPI processes to calculate the quantity $\sqrt{\tilde{h}}$. The next step is to take the time derivative, which is a relatively inexpensive operation, so it is currently only parallelized over the MPI processes and not over OpenMP threads.

The other way generators can join the surface is through crossover points, where non-neighboring generators meet.

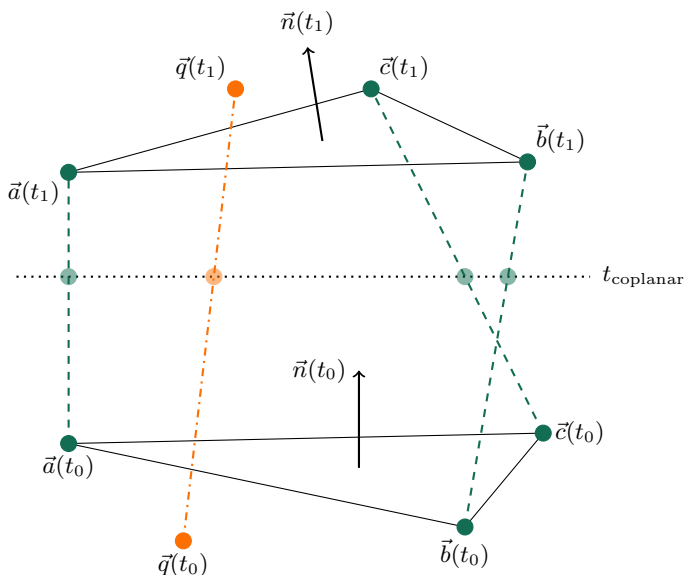


FIG. 6. Checking for the collision of a moving triangle $\triangle abc$ and some other generator $\vec{q}(t)$ between times t_0 and t_1 . The triangle is constructed by connecting three neighboring vertices $\vec{a}(t)$, $\vec{b}(t)$, and $\vec{c}t$. At some time, the four generators may become coplanar, as illustrated in the figure.

Since we are evolving a finite number of generators to approximate the surface, in general the generators we evolve will not cross each other. We therefore look for crossover points by checking for surface self-intersections by using a collision detection algorithm as described in [19], where every vertex is compared against every triangle to see if the generator at that vertex passed through the triangle between neighboring recording times. Our situation is simplified compared to Cohen *et al.* [19], however, because we explicitly start with an unchanging set of triangles as opposed to needing to define and construct a set of triangles from a (θ, ϕ) grid. Because the event horizon surface is approximated by connecting generators to form triangles, the collision of a triangle and any other generator between times t_0 and t_1 indicates that the generator joined the event horizon through a crossover at a time t_{join} satisfying $t_0 \leq t_{\text{join}} < t_1$.

The collision detection algorithm assumes each generator moves linearly through time between two neighboring times, as shown in Fig. 6. The location of a generator $\vec{q}(t)$ is therefore a linear function between t_0 and t_1 ,

$$\forall t \in [t_0, t_1), \quad \vec{q}(t) = \vec{q}(t_0) + \frac{t - t_0}{t_1 - t_0} (\vec{q}(t_1) - \vec{q}(t_0)), \quad (11)$$

and similarly for the vertices of some triangle, $\vec{a}(t)$, $\vec{b}(t)$, and $\vec{c}(t)$. These generators and their trajectories are shown in Fig. 6. The normal vector to the triangle $\triangle abc$ is then a quadratic function in time

$$\vec{n}(t) = \left(\vec{b}(t) - \vec{a}(t) \right) \times \left(\vec{c}(t) - \vec{a}(t) \right). \quad (12)$$

We first solve for all times when the generator $\vec{q}(t)$ and

the triangle are coplanar by finding the roots of

$$\vec{n}(t) \cdot (\vec{q}(t) - \vec{a}(t)) = 0, \quad (13)$$

which is a cubic polynomial. An example of a coplanar time is shown in Fig. 6 as the dotted horizontal line. We immediately disregard any roots of the cubic that lie outside the range $t_0 \leq t_{\text{coplanar}} < t_1$, and disregard complex roots. For every root t_{coplanar} remaining, we check whether $\vec{q}(t_{\text{coplanar}})$ lies inside triangle $\triangle abc$. If so, we mark the time at which the generator joins the horizon as this time, $t_{\text{join}} = t_{\text{coplanar}}$. It is possible that multiple roots of the cubic lie both in the desired time range and inside the triangle, but generators physically cannot cross after they join the horizon [35], so we choose the latest of the t_{coplanar} roots to be the join time.

We apply the collision detection algorithm for every pair of neighboring times where we have recorded generator location data, comparing each triangle to every other vertex. Since all generators of the event horizon are on the event horizon surface at late times, we start with the latest pair of neighboring times and work backwards. Since we are only interested in self-intersections of the actual event horizon surface, we must remove vertices and triangles from the algorithm after they leave the EH backwards in time. Once we find a join time t_{join} for a generator, either corresponding to joining as a caustic or a crossover, we do not need to check for collisions with that generator and other triangles as we move to earlier pairs of times where $t_0 < t_1 < t_{\text{join}}$. Choosing when to remove a triangle from the algorithm is more subtle, since triangles are formed from three EH generators. We only remove a triangle from the algorithm once all three generators forming the triangle have left the EH surface, a choice that is described in Appendix C.

This includes both when the generator would be used to form a triangle as well as when the generator would be the single vertex. If both the caustic and crossover point algorithms determine that $t_a \leq t_{\text{join}} \leq t_b$ for some pair of neighboring times t_a and t_b , then the later time must be the true join time, to satisfy the property that generators do not meet after they join the event horizon.

The search for crossovers is the most costly part of the event horizon simulation, since it is the only part of the simulation that scales quadratically with the number of generators. We have optimized the cost of each individual check for a collision between a vertex and a triangle to $\mathcal{O}(2\mu\text{s})$. In addition, for each pair of neighboring times, we use an OpenMP thread pool to parallelize over the triangles, and we parallelize all the remaining vertices over the MPI processes.

VIII. CONCLUSIONS

In this paper, we have presented a new event horizon finding code, with adaptive localized refinement, based on a Delaunay triangulation on a surface with the topology of a sphere. We now have the ability to refine arbitrary

portions of the event horizon surface to discover and study small-scale features such as the hole in a toroidal event horizon, as discussed in our companion paper [23]. The triangulation is covered by three overlapping coordinate systems to avoid issues with coordinate singularities at the poles of the standard polar coordinate system. Using the backwards geodesic event horizon finding algorithm, we specify how to calculate initial data for event horizon generators and how to use the triangulation when searching for future generators of the event horizon.

There are several ways this event horizon finding code can be further improved. The refinement algorithm currently creates an even distribution of event horizon generators at late times in the BBH simulation, where the horizon looks like Kerr. Unfortunately, when traced backwards in time, the event horizon surface becomes significantly stretched and distorted, leading the triangles and the distribution of generators to be similarly stretched. Since we are interested in studying the event horizon at the time of merger, we would like the generators to be evenly spaced at the time of merger. An improvement to the refinement algorithm would be to first perform an event horizon run using an even distribution of generators to determine how the triangles are stretched near merger, then use the stretch information to add new generators to the initial data surface so that the triangles are initially stretched in the orthogonal direction, but become unstretched near the merger into almost equilateral triangles. It is not obvious to us how to generate such a distribution. We note that it is difficult to re-triangulate the event horizon surface at every time step, because the re-triangulation procedure would need to understand that the surface is stretched, or else it would “cut corners” off the strongly distorted EH shape.

Furthermore, the collision detection algorithm, the slowest step in the EH locating process, is naively $\mathcal{O}(N^2)$ in the number of EH generators. One could improve the coefficient of this algorithm by dividing the space into spatial bins, with a quadtree for example, and ignoring collisions of a triangle and generator in entirely distinct spatial bins. This was not implemented because of the complexity of determining a good splitting of the surface and the problem of handling triangles or vertices that move between different regions.

Appendix A: Null geodesic evolution equations in the 3 + 1 decomposition

It is common for numerical simulations to use the 3 + 1 decomposition [28], so we express the metric Eq. (3) in the form

$$g_{\mu\nu} = \begin{bmatrix} -\alpha^2 + \beta^i \beta_i & \gamma_{ij} \beta^j \\ \gamma_{ij} \beta^j & \gamma_{ij} \end{bmatrix}. \quad (\text{A1})$$

The inverse metric is

$$g^{\mu\nu} = \begin{bmatrix} -\frac{1}{\alpha^2} & \frac{\beta^j}{\alpha^2} \\ \frac{\beta^i}{\alpha^2} & \gamma^{ij} - \frac{\beta^i \beta^j}{\alpha^2} \end{bmatrix}. \quad (\text{A2})$$

The associated connection coefficients for this representation of the metric are

$$\begin{aligned} \Gamma^0_{00} &= \frac{1}{\alpha} (\alpha_{,t} + \beta^k \alpha_{,k} - K_{ij} \beta^i \beta^j) \\ \Gamma^k_{00} &= \gamma^{kj} \left(\beta_{j,t} + \alpha \alpha_{,j} - \frac{1}{2} (\gamma_{mn} \beta^m \beta^n)_{,j} \right) - \beta^k \Gamma^0_{00} \\ \Gamma^0_{i0} &= \frac{1}{\alpha} (\alpha_{,i} - K_{ij} \beta^j) \\ \Gamma^k_{i0} &= -\alpha K_i{}^k + {}^{(3)}\nabla_i \beta^k - \Gamma^0_{i0} \beta^k \\ \Gamma^0_{ij} &= -\frac{1}{\alpha} K_{ij} \\ \Gamma^k_{ij} &= {}^{(3)}\Gamma^k_{ij} + \frac{K_{ij}}{\alpha} \beta^k = {}^{(3)}\Gamma^k_{ij} - \Gamma^0_{ij} \beta^k, \end{aligned} \quad (\text{A3})$$

where ${}^{(3)}\nabla_i$ and ${}^{(3)}\Gamma^k_{ij}$ are the covariant derivative and connection coefficients associated with the spatial metric γ_{ij} , and we have used the extrinsic curvature

$$K_{ij} = \frac{1}{2\alpha} (-\gamma_{ij,t} + 2\gamma_{ik} \beta^k_{,j} + \gamma_{ij,m} \beta^m). \quad (\text{A4})$$

To numerically integrate the geodesic equation

$$\frac{d^2 x^\tau}{d\lambda^2} + \Gamma^\tau_{\mu\nu} \frac{dx^\mu}{d\lambda} \frac{dx^\nu}{d\lambda} = 0, \quad (\text{A5})$$

we seek an efficient splitting into two first-order differential equations. A natural splitting arises through the use of the photon momentum

$$p^\mu = \frac{dx^\mu}{d\lambda}. \quad (\text{A6})$$

With this momentum variable, we have the evolution equations

$$\frac{dp^\tau}{d\lambda} = -\Gamma^\tau_{\mu\nu} p^\mu p^\nu \quad (\text{A7a})$$

$$\frac{dx^\tau}{d\lambda} = p^\tau. \quad (\text{A7b})$$

These can be converted to equations with respect to a coordinate time t by dividing through by $p^0 = dt/d\lambda$.

Cohen *et al.* [18] use a similar form by evolving the quantity p^i/p^0 as an intermediate variable, although they define the variable p^i to be what is called p^i/p^0 here. This intermediate variable gives the evolution equations

$$\frac{d}{dt} \left(\frac{p^i}{p^0} \right) = \left(\Gamma^0_{\mu\nu} \frac{p^i}{p^0} - \Gamma^i_{\mu\nu} \right) \frac{p^\mu}{p^0} \frac{p^\nu}{p^0} \quad (\text{A8a})$$

$$\frac{dx^i}{dt} = \frac{p^i}{p^0}, \quad (\text{A8b})$$

which is a convenient intermediate variable choice as we will see shortly, but is problematic because it involves all of the connection coefficients during evolution. Additionally, the use of Γ^μ_{00} involves time derivatives of the lapse and shift (Eq. (A3)).

Performing the sum over all the connection coefficients is inefficient because of the number of terms being summed as well as inaccurate if the metric terms come from a numerical source versus an analytic source. There are many cancellations in the geodesic equation that can be taken advantage of with the appropriate choice of intermediate variable. Hughes et al. [15] explored using

$$p_\mu = g_{\mu\nu} p^\nu, \quad (\text{A9})$$

obtaining the evolution equations

$$\frac{dp_i}{d\lambda} = -\alpha\alpha_{,i}(p^0)^2 + \beta^k{}_{,i} p_k p^0 - \frac{1}{2}\gamma^{jk}{}_{,i} p_j p_k \quad (\text{A10a})$$

$$\frac{dx^i}{d\lambda} = \gamma^{ij} p_j - \beta^i p^0. \quad (\text{A10b})$$

Converting to an evolution with respect to coordinate time t gives

$$\frac{dp_i}{dt} = -\alpha\alpha_{,i} p^0 + \beta^k{}_{,i} p_k - \frac{1}{2}\gamma^{jk}{}_{,i} \frac{p_j p_k}{p^0} \quad (\text{A11a})$$

$$\frac{dx^i}{dt} = \gamma^{ij} \frac{p_j}{p^0} - \beta^i. \quad (\text{A11b})$$

These equations have considerably fewer terms than those in Eq. (A8b) and also no time derivatives of metric functions. We note that although the variable p^0 is not evolved, it can be calculated by enforcing $\vec{p} \cdot \vec{p} = 0$, giving $p^0 = \sqrt{\gamma^{ij} p_i p_j} / \alpha$.

Unfortunately, these equations are poorly suited for evolving outgoing null geodesics near black hole horizons in the coordinate systems we are interested in, as $p^0 \sim e^t$ for an event horizon generator of a Schwarzschild spacetime expressed in Kerr-Schild coordinates for example. Other components of the 4-momentum have similar exponential dependence, leading to increasingly small timesteps. The evolution equations in Eq. (A8b) conveniently cancel the exponential behavior by evolving the ratio p^i / p^0 . Can we get the best of both worlds, avoiding the exponential behavior of Eq. (A11b) and avoiding the large number of terms in Eq. (A8b)?

One attempt is to evolve the lower momentum normalized by p^0 as in

$$P_i \equiv \frac{p_i}{p^0}. \quad (\text{A12})$$

With the definition $P^i = \gamma^{ij} P_j$, this yields the evolution equations

$$\frac{dP_i}{dt} = -\alpha\alpha_{,i} + \beta^k{}_{,i} P_k - \frac{1}{2}\gamma^{jk}{}_{,i} P_j P_k + \frac{P_i}{\alpha} (-\alpha_{,j}\beta^j + 2\alpha_{,j} P^j + \dot{\alpha} - K_{jk} P^j P^k) \quad (\text{A13a})$$

$$\frac{dx^i}{dt} = P^i - \beta^i \quad (\text{A13b})$$

These equations certainly have more terms than Eq. (A11b), but do not suffer from the issue of small timesteps.

We can reduce the number of terms involved in the equations further by including an extra factor of the lapse,

such that

$$\Pi_i \equiv \frac{p_i}{\alpha p^0} = \frac{P_i}{\alpha} = \frac{p_i}{\sqrt{\gamma^{jk} p_j p_k}}. \quad (\text{A14})$$

Similarly, we define $\Pi^i = \gamma^{ij} \Pi_j$. The resulting evolution equations are those mentioned in the main text, which we repeat here for completeness

$$\frac{d\Pi_i}{dt} = -\alpha_{,i} + (\alpha_{,j} \Pi^j - \alpha K_{jk} \Pi^j \Pi^k) \Pi_i + \beta^k{}_{,i} \Pi_k - \frac{1}{2}\alpha\gamma^{jk}{}_{,i} \Pi_j \Pi_k \quad (\text{A15a})$$

$$\frac{dx^i}{dt} = \alpha \Pi^i - \beta^i. \quad (\text{A15b})$$

By using the variable Π_i , we have reduced further the

number of terms involved, eliminated time derivatives of

the metric, as well as removed the small timestep behavior. Since we are evolving a normalized momentum, we have lost the ability to calculate p^0 . If p^0 is necessary it can be evolved separately, but for outgoing geodesics near black hole horizons $p^0 \sim e^t$. For such geodesics, we recommend evolving the quantity $\ln(\alpha p^0)$, giving

$$\frac{d \ln(\alpha p^0)}{dt} = -\alpha_{,i} \Pi^i + \alpha K_{ij} \Pi^i \Pi^j. \quad (\text{A16})$$

An alternative is to simply evolve $\ln(p^0)$, which has more terms. For geodesics evolved far from black hole horizons, p^0 can be evolved directly by noting $d \ln(p^0)/dt = (1/p^0) (dp^0/dt)$.

The evolution equations using Π_i are similar to those in Equation (28) of Vincent *et al.* [33]. In fact, the intermediate evolution variable Π_i is related to their variable V^i by the three-metric, such that $\Pi^i = V^i$. But our Eq. (6b) has a reduced number of both temporal and spatial derivatives of metric quantities compared to Vincent's Eq. (28).

Appendix B: Spacetime interpolations

Each component of the metric is handled independently, so it is sufficient to consider the interpolation of a scalar A defined on a set of points split into separate subdomains and on a set of time slices. This is complicated by the fact that SPEC utilizes a dual-frame system [31, 36], where computations are performed in a reference frame called the grid frame. In the grid frame, the black holes are stationary with respect to the collocation points of the evolution, and a time-dependent mapping is maintained between this frame and the asymptotically inertial frame, which we call the inertial frame.

In the inertial frame, the grid points on which the scalar A is defined are moving with respect to time, as seen in Fig. 7. As a consequence, the domain boundary that is stationary in the grid frame is also moving with time. Suppose we are interested in the value of A at the \times , located at (x_1^i, t) where x_1^i is the spatial location in the inertial frame, and we want to use 6 time slices to perform a 5th order time interpolation. If we choose to perform a spatial interpolation on each of the 6 time slices first, then perform a temporal interpolation to the time t , then we have two choices for how to spatially interpolate.

The first choice, shown with pluses and a line in purple, is to spatially interpolate to x_1^i on each time slice, then interpolate in time. This method has two major drawbacks. The scalar A is, by construction, usually varying slower in time when viewed at a constant grid point x_G^i compared to a constant inertial point x_1^i . The result is less accurate temporal interpolations along x_1^i which leads to decreased time step sizes. In addition, spatially interpolating to a constant point in the inertial frame could lead to attempting to spatially interpolate outside of the domain, as seen on the last time slice on the right side of the figure. Therefore, the preferred option is to

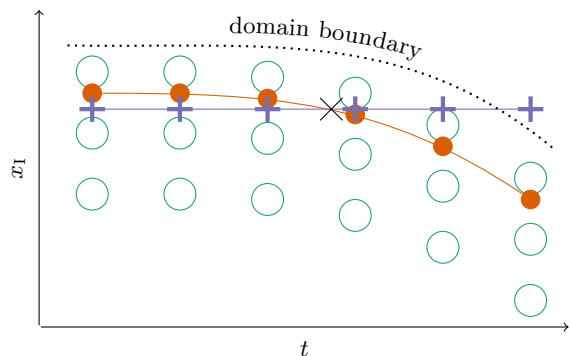


FIG. 7. Spacetime interpolation to the black \times , as viewed in the inertial frame of SPEC. The green circles represent the grid points of the BBH simulation at the times where metric data was stored to disk. The dotted line corresponds to the domain boundary of the simulation. If we first perform a set of spatial interpolations, then interpolate the results in time, we have two choices for how to handle these interpolations. One choice is to interpolate to a constant location in the grid frame shown in orange, or a constant location in the inertial frame shown in purple. The grid frame interpolation is advantageous for multiple reasons.

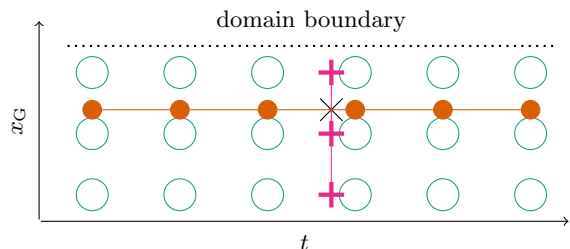


FIG. 8. Spacetime interpolation to the black \times , as viewed in the grid frame of SPEC. The setup is similar to Fig. 7, but we are observing in the grid frame. We demonstrate the additional choice between performing the spatial interpolations before or after temporal interpolations. Spatial before temporal is shown in orange, and temporal before spatial is shown in pink.

interpolate to a constant grid frame point on each time slice, then interpolate in time, as shown with filled dots and a line in orange.

It is instructive to view this interpolation in the grid frame, as seen in Fig. 8. In this frame, the locations of the domain boundary and the grid points are stationary in time. On each time slice, we perform a spatial interpolation to the orange points at $x_G^i = M(x_1^i, t)$, where t is the time to which we are interpolating and M is the time dependent mapping from the inertial frame to the grid frame. In this figure, we show another possibility where we first interpolate in time along each grid point in the subdomain to the pink pluses, then perform a spatial interpolation. If we count the number of operations required for either method, we find that interpolating in time then space takes $\mathcal{O}(N_s N_t^2 + N_s^2)$ operations, where N_s is the number of spatial points in the subdomain and N_t is the number of time slices used in the interpolation.

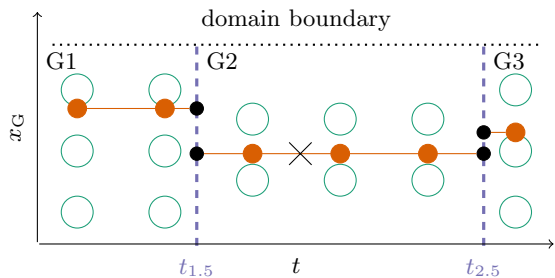


FIG. 9. Spacetime interpolation to the black \times , as viewed in the grid frame of SPEC, showing spatial before temporal interpolation and constant grid location interpolation. The setup is similar to Fig. 8, but we now have AMR. The vertical dashed purple lines correspond to AMR regrids, where the grid in general is quite different before and after the regrid. When we encounter a regrid, we must find the relationship between the regrids at the black dot locations by using the inertial frame which is continuous across regrids, as seen in Fig. 10.

Interpolating in space then time takes $\mathcal{O}(N_t N_s^2 + N_t^2)$ operations, which is typically larger than the number of operations when interpolating in time first, since $N_s > N_t$ for our case.

Unfortunately, while interpolating in time before space requires fewer operations, in practice the error in the interpolated tensors is larger, resulting in the generator timestepper taking smaller steps. We therefore default to always performing a spectral spatial interpolation on each time slice to the grid point x_G^i , then interpolating in time with Lagrange polynomial interpolation.

The situation becomes more complicated when adaptive mesh refinement (AMR) during the original BBH evolution alters the grid frame. In general, the evolution grid has a different number of points after an AMR regrid, and the coordinates in the grid frame are not continuous across the regrid. In Fig. 9, we see two AMR regrids denoted by vertical dashed lines at times $t_{1.5}$ and $t_{2.5}$. We start in the grid frame labeled G2, where the desired interpolation location (x_G^i, t) lives, following the same procedure of mapping to the grid frame location $x_{G2}^i = M_2(x_G^i, t)$, where M_2 is the mapping from the inertial frame to the grid frame G2. We spatially interpolate to the grid point x_{G2}^i at all the times within the time interpolation stencil and in the frame G2. When a regrid occurs, we must determine how the two neighboring grid frames are related so we know to what grid location to interpolate. Specifically, we need to know what the corresponding grid frame locations in G1 and G3 are, that is, x_{G1}^i and x_{G3}^i respectively.

We make use of the inertial frame whose coordinates are continuous across the regrid to find the relationship between the grid frames. Consider the regrid at $t_{1.5}$. We map from the G2 grid frame location to the inertial frame via the G2 mapping $M_2^{-1}(x_{G2}^i, t_{1.5})$, then map from the inertial frame to the G1 grid to find the corresponding grid location x_{G1}^i . Therefore, the relationship between

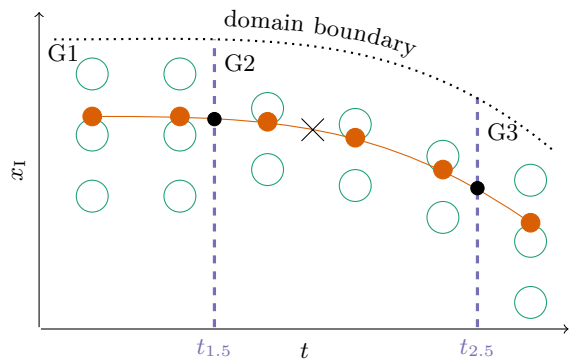


FIG. 10. Spacetime interpolation to the black \times as in Fig. 9, but viewed in the inertial frame of SPEC. The line along which we are interpolating is continuous in the inertial frame, and the black dots on the boundary between regrids are used to find how the neighboring grid frames are related.

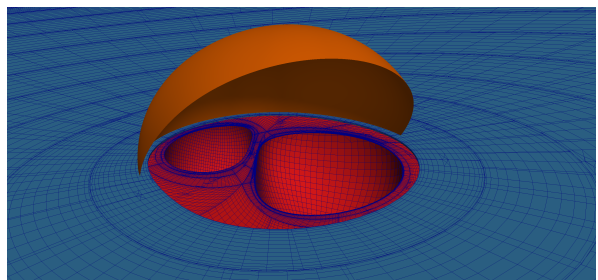


FIG. 11. Portion of the event horizon surface, shown in orange, on top of the SPEC domain structure just before and after the grid change for the ringdown. In red, we see the evolution grid just before the ringdown grid change including the excision regions associated with the two inner apparent horizons. In blue, we see the evolution grid just after the ringdown grid change, with only one excision region associated with the common apparent horizon. Both the inner and common apparent horizons can be seen in panel (d) of Fig. 1.

the grid locations is

$$x_{G1}^i = M_1(M_2^{-1}(x_{G2}^i, t_{1.5}), t_{1.5}). \quad (\text{B1})$$

This procedure is applied at every regrid in the range of times where temporal interpolation occurs. The result is a set of straight lines in the grid frame shown in Fig. 9 along which we interpolate in time.

The corresponding inertial frame viewpoint is shown in Fig. 10. Again we see that the domain boundary and grid points are in general at different locations in the inertial frame, but the line along which we are interpolating is continuous across the regrids unlike in the grid frame. The black dot at each regrid time is used as the anchor point to map between the neighboring grid frames in Eq. (B1). Specifically, the black dot along the first regrid satisfies

$$M_1^{-1}(x_{G1}^i, t_{1.5}) = M_2^{-1}(x_{G2}^i, t_{1.5}). \quad (\text{B2})$$

There is an additional complication to this procedure, albeit rare, that can occur when determining the rela-

relationship between neighboring grid frames in Eq. (B1). In Fig. 11, we see part of the domain structure for a BBH simulation with parameters consistent with the Advanced LIGO event [1], specifically $m_1/m_2 = 1.25$ with dimensionless spin magnitudes $\chi_1 = 0.45$, $\chi_2 = 0.54$ in arbitrary directions. In red, we see a cutaway of the inspiral domain structure just before the domain topology changes for the ringdown, where there are two excision regions associated with individual apparent horizons of the black holes. At this time, SPEC finds a common apparent horizon encapsulating both of the inner apparent horizons, which triggers the evolution domain to change topology to have just one excision region. The new domain structure after the regrid is shown in blue, so all the structure near the inner apparent horizons shown in red has been excised from the domain. Finally, in orange, we show a portion of the event horizon surface. Since the apparent horizon by construction is always inside the event horizon, the event horizon surface always encapsulates the excision region completely.

Consider the transition between G2 to G3 in Fig. 10, and assume that this transition is associated with the domain change from the red inspiral grid to the blue ringdown grid. If the point to which we want to interpolate resides in the red region after the regrid, then the point will be off the domain, causing the interpolation to fail. In SPEC, regrids can only cause grid locations to be removed from the evolution grid, not to enter the evolution grid. Therefore, we use a lopsided time interpolation stencil favoring earlier time slices to solve this issue. We first try a balanced stencil with $n/2$ times on either side of the desired interpolation point, and retry with $n/2 + 1$ times before the point and $n/2 - 1$ after if it fails, and so forth.

While we have the ability to perform spacetime interpolations in multiple ways, the default is to interpolate first in space to a constant point in the grid frame on each time slice required for the time interpolation, then perform the time interpolation. The primary advantages to these choices are that the code handles interpolation requests accurately and without failure near domain boundaries and AMR regrids.

Appendix C: Removing triangles from the collision detection algorithm

When tracing event horizon generators backwards through time, generators leave the EH surface when they meet other generators. These meeting points are classified as either caustics where neighboring generators meet or crossover points where non-neighboring generators meet. We detect crossover points by searching for EH surface self-intersections where in theory two generators cross, but in practice we only identify that a generator q intersected a triangle Δabc between neighboring times t_0 and t_1 as described in Section VII. This collision implies there is some EH generator u (that we have not evolved) inside

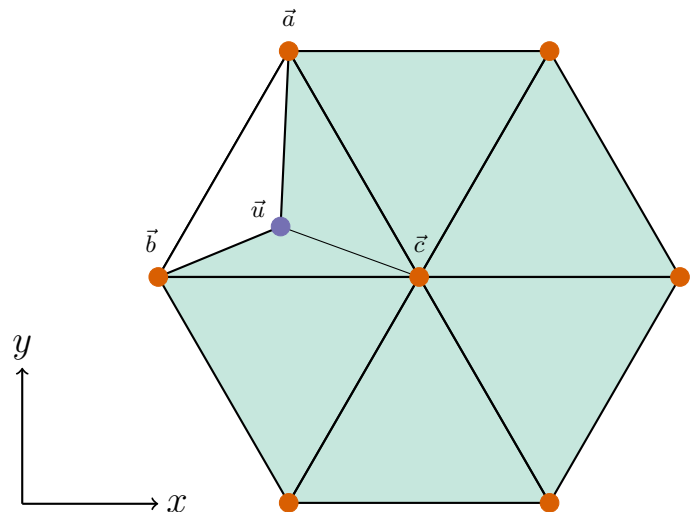


FIG. 12. A portion of a null plane wave, with normal out of the page, approximated by a set of null generators shown as orange dots. This null plane wave and another null plane wave, not shown, connect to form a toy event horizon used to study the collision detection algorithm. The shaded blue-green triangles are filled with future generators of this toy event horizon, where a hypothetical generator of the EH shown as a purple dot, u , has just converted from a future generator to a true generator at this time.

Δabc that met with q between t_0 and t_1 , so we flag q as leaving the horizon backwards through time.

Consider the setup in Fig. 12 where we follow part of a null plane wave satisfying $t = z$ approximated by a set of generators in orange dots connected to form a set of triangles. Another null plane wave, not shown, satisfies $t = (x - y - z)/\sqrt{3}$ and is similarly approximated by a set of generators. On small scales, these two intersecting plane waves roughly approximate two intersecting portions of the EH surface. We want to search for intersections of these plane waves using only the generators of the plane waves we are evolving. We know analytically that the intersection of these waves in the plane of Fig. 12 satisfies $t = (x - y)/(1 + \sqrt{3})$ and so travels in the $(+x, -y)$ direction forwards in time (and travels faster than the speed of light). After the two waves intersect, the future generators shaded with blue-green will join the event horizon. At this particular time, a generator of the plane wave not shown in this figure, q , intersects Δabc at the location u , so a generator at u would join the horizon at this instant along with q .

As was done in Section VII, the algorithm is to follow both plane waves backwards through time to search for intersections where generators leave the surface. We need to identify for each generator we keep track of, shown as an orange dot, when the generator leaves the horizon. One way to handle the fact that the generator q intersected a hypothetical generator at u is to actually create a new generator at u and keep track of it. As shown in Fig. 12, we would then classify Δacu and Δucb as being filled

with future generators, and $\triangle abc$ would still be part of the EH surface. We should therefore remove $\triangle acu$ and $\triangle ucb$ from the collision detection algorithm, and leave $\triangle acb$ in the algorithm, because we only want to detect collisions between generators that are both on the EH.

This method would give a correct algorithm, but introduces some additional complications, so we seek a simpler algorithm. Without adding a generator, is it better to continue to include $\triangle abc$ in the algorithm or remove it from the algorithm? Both choices have some potential failure modes we need to consider. If we continue to include the triangle in the collision detection, then the potential failure mode occurs when some generator w intersects either $\triangle acu$ or $\triangle ucb$, and we proceed to incorrectly flag w as having left the EH backwards in time. The generator w should still be considered part of the EH surface because we only care about surface self-intersections between two generators that are both on the EH. However, in this setup of two colliding plane waves, there will never be such a generator w that is falsely flagged, because the plane wave to which w belongs has already passed by the triangles $\triangle acu$ and $\triangle ucb$. Therefore, including the full triangle $\triangle abc$ in the collision detection algorithm introduces no failure modes that are possible if the EH is sufficiently covered with generators.

The other option is to remove $\triangle abc$ from the algorithm. The potential failure mode here occurs when a generator w should have intersected some generator in $\triangle abc$ causing it to leave the horizon, but we incorrectly label w as still being a part of the EH surface. This failure mode can and does occur in both this toy model example and in realistic BBH event horizon simulations. Therefore, removing the triangle from the collision detection yields incorrect results, where some generators are falsely flagged as being on the EH.

To summarize, the method we use is to keep $\triangle abc$ in the collision detection algorithm until the entire triangle is filled with future generators, or equivalently when all three generators a , b , and c are all flagged as future generators of the EH. If all three generators that form the triangle

are future generators, the triangle must be removed from the algorithm. This is because the approximation of two intersecting plane waves breaks down on large or long timescales, so it is possible for the triangle of future generators to wrap back toward the EH as we trace it backwards through time. If the triangle is never removed from the algorithm, then we see some future generator triangles intersecting with generators on the EH surface, resulting in unphysical holes in the event horizon.

ACKNOWLEDGMENTS

We thank David Nichols for useful conversations about affine parametrizations of event horizon generators. We are grateful to François Hébert and William Throwe for various helpful conversations including numerous triangle drawing whiteboard sessions. We thank Daniel A. Hemberger for helping us understand the intricacies of the adaptive mesh refinement in SPEC. For helping smooth the visualization of event horizon surfaces, we thank Curran D. Muhlberger. We also thank Harald Pfeiffer for providing the BBH simulation with parameters similar to the system detected by Advanced LIGO, shown in Fig. 11. For providing useful suggestions during the writing phase, we thank Nils Deppe.

We gratefully acknowledge support for this research at Cornell from the Sherman Fairchild Foundation and NSF grants PHY-1306125 and AST-1333129. Calculations were performed on the Zwicky cluster at Caltech, which is supported by the Sherman Fairchild Foundation and by NSF award PHY-0960291; on the NFS XSEDE network under grant TG-PHY990007N; at the GPC supercomputer at the SciNet HPC Consortium [37]; SciNet is funded by: the Canada Foundation for Innovation (CFI) under the auspices of Compute Canada; the Government of Ontario; Ontario Research Fund (ORF) Research Excellence; and the University of Toronto. All the surface visualizations were done using Paraview [38].

-
- [1] B. P. Abbott *et al.* (Virgo, LIGO Scientific), *Phys. Rev. Lett.* **116**, 061102 (2016), [arXiv:1602.03837 \[gr-qc\]](#).
 - [2] B. P. Abbott *et al.* (LIGO Scientific Collaboration, Virgo Collaboration), (2016), [arXiv:1602.03841 \[gr-qc\]](#).
 - [3] L. Pekowsky, R. O’Shaughnessy, J. Healy, and D. Shoemaker, *Phys. Rev. D* **88**, 024040 (2013), [arXiv:1304.3176 \[gr-qc\]](#).
 - [4] <http://www.black-holes.org/waveforms>.
 - [5] P. Ajith, M. Boyle, D. A. Brown, B. Brügmann, L. T. Buchman, *et al.*, *Class. Quantum Grav.* **29**, 124001 (2012).
 - [6] Y. Zlochower and C. O. Lousto, *Phys. Rev. D* **92**, 024022 (2015).
 - [7] B. Brügmann, J. A. González, M. Hannam, S. Husa, U. Sperhake, and W. Tichy, *Phys. Rev. D* **77**, 024027 (2008), [gr-qc/0610128](#).
 - [8] K. Jani, J. Healy, J. A. Clark, L. London, P. Laguna, and D. Shoemaker, (2016), [arXiv:1605.03204 \[gr-qc\]](#).
 - [9] E. Poisson, *A Relativist’s Toolkit: The Mathematics of Black-Hole Mechanics* (Cambridge University Press, 2004).
 - [10] R. Penrose, pp 121-235 of *Battelle Rencontres*. DeWitt, Cecile M. (ed.). New York W. A. Benjamin, Inc. (1968).
 - [11] S. W. Hawking and G. F. R. Ellis, *The Large Scale Structure of Space-time* (Cambridge University Press, Cambridge, England, 1973).
 - [12] R. M. Wald, *General Relativity* (University of Chicago Press, Chicago, IL, 1984).
 - [13] P. Anninos, D. Bernstein, S. Brandt, J. Libson, J. Massó, E. Seidel, L. Smarr, W.-M. Suen, and P. Walker, *Phys. Rev. Lett.* **74**, 630 (1995).
 - [14] S. L. Shapiro and S. A. Teukolsky, *Astrophys. J.* **235**, 199 (1980).

- [15] S. A. Hughes, C. R. Keeton, P. Walker, K. T. Walsh, S. L. Shapiro, and S. A. Teukolsky, *Phys. Rev. D* **49**, 4004 (1994).
- [16] S. L. Shapiro, S. A. Teukolsky, and J. Winicour, *Phys. Rev. D* **52**, 6982 (1995).
- [17] J. Libson, J. Massó, E. Seidel, W.-M. Suen, and P. Walker, *Phys. Rev. D* **53**, 4335 (1996).
- [18] M. Cohen, H. P. Pfeiffer, and M. A. Scheel, *Class. Quantum Grav.* **26**, 035005 (2009), [arXiv:0809.2628](https://arxiv.org/abs/0809.2628).
- [19] M. I. Cohen, J. D. Kaplan, and M. A. Scheel, *Phys. Rev. D* **85**, 024031 (2012), [arXiv:1110.1668](https://arxiv.org/abs/1110.1668) [gr-qc].
- [20] M. Siino, *Phys. Rev. D* **58**, 104016 (1998).
- [21] S. Husa and J. Winicour, *Phys. Rev. D* **60**, 084019 (1999), [gr-qc/9905039](https://arxiv.org/abs/gr-qc/9905039).
- [22] L. Lehner, N. Bishop, R. Gomez, B. Szilágyi, and J. Winicour, *Phys. Rev. D* **60**, 044005 (1999), [arXiv:9809034](https://arxiv.org/abs/9809034) [gr-qc].
- [23] A. Bohn, L. E. Kidder, and S. A. Teukolsky, (2016).
- [24] B. Delaunay, *Bulletin de l'Académie des Sciences de l'URSS. Classe des sciences mathématiques et na*, 793 (1934).
- [25] W. H. Press, S. A. Teukolsky, W. T. Vetterling, and B. P. Flannery, *Numerical Recipes: The Art of Scientific Computing (3rd Ed.)* (Cambridge University Press, New York, 2007).
- [26] K. Thorne, Suggestion to the authors of [13, 17] that the locus of all event horizon generators forms at all times a smooth and sometimes self-intersecting surface.
- [27] W. C. Thacker, *J. Phys. Oceanogr.* **7**, 284 (1977).
- [28] R. Arnowitt, S. Deser, and C. W. Misner, in *Gravitation: An Introduction to Current Research*, edited by L. Witten (Wiley, New York, 1962) pp. 227–265, [gr-qc/0405109](https://arxiv.org/abs/gr-qc/0405109).
- [29] <http://www.black-holes.org/SpEC.html>.
- [30] B. Szilágyi, L. Lindblom, and M. A. Scheel, *Phys. Rev. D* **80**, 124010 (2009), [arXiv:0909.3557](https://arxiv.org/abs/0909.3557) [gr-qc].
- [31] D. A. Hemberger, M. A. Scheel, L. E. Kidder, B. Szilágyi, G. Lovelace, N. W. Taylor, and S. A. Teukolsky, *Class. Quantum Grav.* **30**, 115001 (2013), [arXiv:1211.6079](https://arxiv.org/abs/1211.6079) [gr-qc].
- [32] A. Bohn, W. Throwe, F. Hébert, K. Henriksson, D. Bunnadar, M. A. Scheel, and N. W. Taylor, *Class. Quantum Grav.* **32**, 065002 (2015).
- [33] F. Vincent, E. Gourgoulhon, and J. Novak, *Class. Quantum Grav.* **29**, 245005 (2012).
- [34] T. W. Baumgarte, G. B. Cook, M. A. Scheel, S. L. Shapiro, and S. A. Teukolsky, *Phys. Rev. D* **54**, 4849 (1996).
- [35] C. W. Misner, K. S. Thorne, and J. A. Wheeler, *Gravitation* (Freeman, New York, New York, 1973).
- [36] M. A. Scheel, H. P. Pfeiffer, L. Lindblom, L. E. Kidder, O. Rinne, and S. A. Teukolsky, *Phys. Rev. D* **74**, 104006 (2006).
- [37] C. Loken, D. Gruner, L. Groer, R. Peltier, N. Bunn, M. Craig, T. Henriques, J. Dempsey, C.-H. Yu, J. Chen, L. J. Dursi, J. Chong, S. Northrup, J. Pinto, N. Knecht, and R. V. Zon, *J. Phys.: Conf. Ser.* **256**, 012026 (2010).
- [38] “ParaView - open source scientific visualization,” <http://www.paraview.org/>.